Electronic Supplementary Material (ESI) for Dalton Transactions.

Supporting information: Anionic Ordering in $Pb_2Ti_4O_9F_2$ Revisited by Nuclear Magnetic Resonance and Density Functional Theory

Kengo Oka,[*,†,‡] Tom Ichibha,[*,¶,‡] Daichi Kato,[§] Yasuto Noda,[‖] Yusuke Tominaga,[‖] Kosei Yamada,[†] Mitsunobu Iwasaki,[†] Naoki Noma,[⊥] Kenta Hongo,[#] Ryo Maezono,[@] and Fernando A. Reboredo[¶]

†*Department of Applied Chemistry, Faculty of Science and Engineering, Kindai University, Higashiosaka, Osaka 577-8502, Japan*

‡*These two authors contributed equally.*

¶*Materials Science and Technology Division, Oak Ridge National Laboratory, Oak Ridge, Tennessee 37831, USA*

§*Department of Energy and Hydrocarbon Chemistry, Graduate School of Engineering, Kyoto University, Kyoto 615-8510, Japan*

‖*Division of Chemistry, Graduate School of Science, Kyoto University, 606-8502 Kyoto, Japan*

⊥*Joint Research Center, Kindai University, Higashiosaka, Osaka 577-8502, Japan*

#*Research Center for Advanced Computing Infrastructure, JAIST, Asahidai 1-1, Nomi, Ishikawa 923-1292, Japan*

@*School of Information Science, JAIST, Asahidai 1-1, Nomi, Ishikawa 923-1292, Japan*

E-mail: koka@apch.kindai.ac.jp; ichibha@icloud.com

Experimental crystal structures

The synchrotron X-ray powder diffraction (SXRD) patterns of the $Pb_2Ti_4O_9F_2$ (300 K) and the high temperature (600 K) and low temperature (300 K) structures of $Bi_2Ti_4O_{11}$ are shown in Figure S1. The crystallographic parameters determined by the Rietveld refinement are shown in Tables S1–S3. The structures are attached in the CIF format. The file names are 2191023_Pb2Ti4O9F2_300K.cif, 2159898_Bi2Ti4O11_600K.cif, and 2159899_Bi2Ti4O11_300K.cif. In the CIF files, O1–O6 correspond to the O atoms at the site 1–6. F5 and F6 correspond to the F atoms at the site 5 and 6. The crystal structures are visualized in Figure S2 with the anion site numbers.

Table S1: $Pb_2Ti_4O_9F_2$ (300 K): Space group $C2/m$ (No. 12), Z=2, a=14.6263(11) Å, b=3.8279(1) Å, c=10.7526(8) Å, β=135.577(3)°, V=421.38(5) $Å^3$, R_{WP}=3.77 %, R_I=1.90 %. The B parameters for the anion sites are restrained to be equal.

atom	g	site	x	y	z	B ($Å^2$)
Pb1	1	4i	0.2416(1)	0	0.1556(1)	1.17(2)
Ti1	1	4i	0.4471(3)	0	0.7835(4)	0.96(6)
Ti2	1	4i	0.0770(3)	0	0.4567(3)	0.19(6)
O1	1	4i	0.4531(8)	0.5	0.7541(10)	0.65(8)
O2	1	4i	0.4232(6)	0	0.5713(9)	0.65
O3	1	2b	0.5	0	0	0.65
O4	1	4i	0.5990(7)	0.5	0.6588(10)	0.65
O5	0.73	4i	0.2718(7)	0	0.6489(10)	0.65
F5	0.27	4i	0.2718	0	0.6489	0.65
O6	0.27	4i	0.6457(6)	0	0.9330(9)	0.65
F6	0.73	4i	0.6457	0	0.933	0.65

Electronic density of $Pb_2Ti_4O_9F_2$ and $Bi_2Ti_4O_{11}$

Figure S3 shows the electron density distribution obtained by MEM. Comparing the isostructural $Pb_2Ti_4O_9F_2$ (300 K) and $Bi_2Ti_4O_{11}$ (600 K), the Bi-O6 are more covalent bonding than Pb-O/F6 because Bi prefers more positive charge state (+3) than Pb (+2). This is considered to be a reason of less symmetric structure of $Bi_2Ti_4O_{11}$ than $Pb_2Ti_4O_9F_2$. The differences of covalent character of the Bi-O6 bonds between the high and low temperature phases of $Bi_2Ti_4O_{11}$ are obvious. This

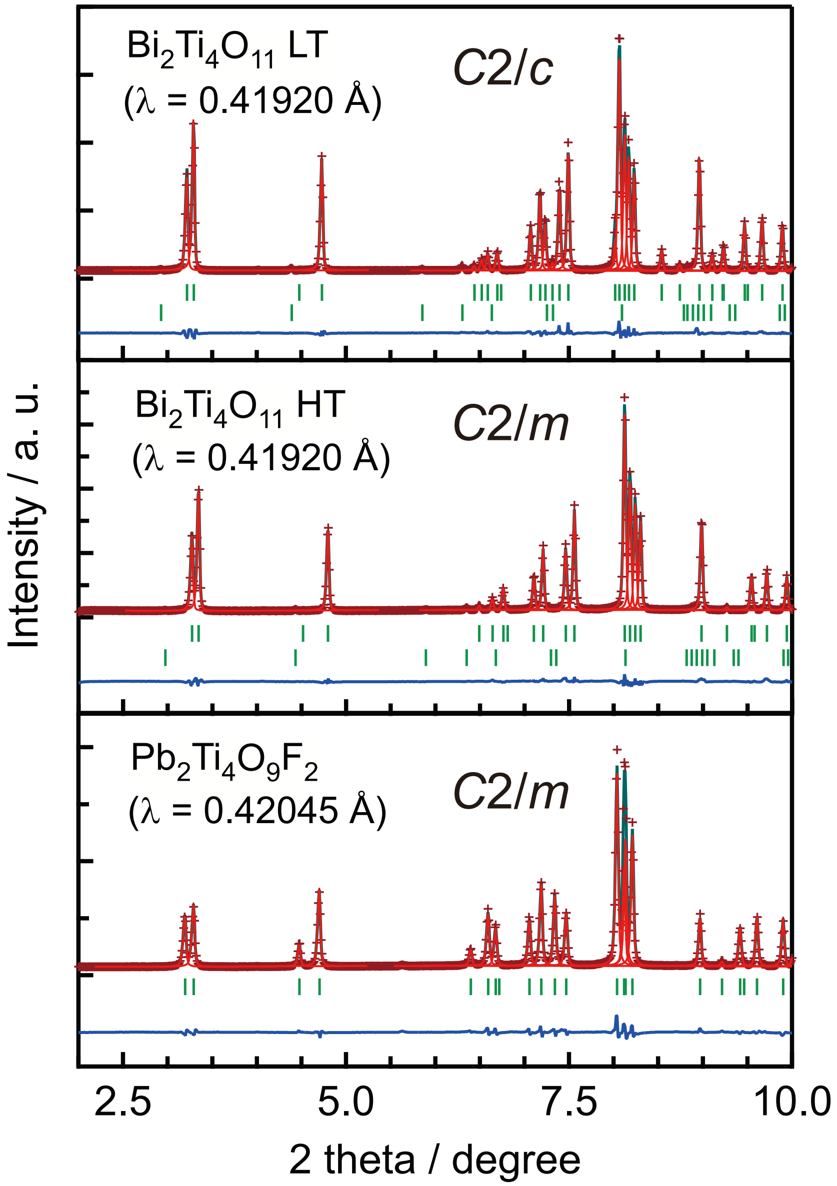

Figure S1: Structural characterization of $Pb_2Ti_4O_9F_2$ and $Bi_2Ti_4O_{11}$ by Rietveld refinement using the SXRD patterns. The red crosses, black solid line, and blue solid line respectively represent the observed, calculated, and difference intensities. The green ticks indicate the positions of the Bragg peaks. The second green ticks appeared in the patterns for $Bi_2Ti_4O_{11}$ LT and HT phases indicate the Bragg peaks of $Bi_4Ti_3O_{12}$, which is an impurity phase. Presence of 2 wt% of $Bi_4Ti_3O_{12}$ was indicated by the Rietveld refinements for $Bi_2Ti_4O_{11}$.

Table S2: $Bi_2Ti_4O_{11}$ (600 K): Space group $C2/m$ (No. 12), Z=2, a=14.6357(3) Å, b=3.8030(1) Å, c=10.7823(3) Å, β=136.122(1)°, V=415.97(2) Å^3, R_{WP}=3.49 %, $\mathrm{R_I}$= 3.27 %. The B parameters for the anion sites are restrained to be equal.

atom	g	site	x	y	z	B (Å^2)
Bi1	1	4i	0.2511(1)	0	0.1423(1)	2.01(2)
Ti1	1	4i	0.4444(2)	0	0.7823(3)	0.41(6)
Ti2	1	4i	0.0857(3)	0	0.4644(3)	0.49(5)
O1	1	4i	0.4594(7)	0.5	0.7595(9)	1.15(10)
O2	1	4i	0.4253(7)	0	0.5726(10)	1.15
O3	1	2b	0.5	0	0	1.15
O4	1	4i	0.6042(7)	0.5	0.6659(9)	1.15
O5	1	4i	0.2722(8)	0	0.6448(11)	1.15
O6	1	4i	0.6601(7)	0	0.9547(10)	1.15

Table S3: $Bi_2Ti_4O_{11}$ (300 K): Space group $C2/c$ (No. 15), Z=4, a=14.6047(3) Å, b=3.8072(1) Å, c=14.9480(2) Å, β=93.145(1)°, V=829.89(2) Å^3, R_{WP}=2.52 %, $\mathrm{R_I}$=1.17 %. The B parameters for the anion sites are restrained to be equal.

atom	g	site	x	y	z	B (Å^2)
Bi1	1	8f	0.3213(1)	0.3255(1)	0.1796(1)	0.43(2)
Ti1	1	8f	0.0534(1)	0.2492(5)	0.1407(1)	0.10(4)
Ti2	1	8f	0.1463(1)	0.7404(5)	0.0171(1)	0.04(9)
O1	1	8f	0.0784(3)	0.750(1)	0.1286(3)	0.48(6)
O2	1	8f	0.1369(5)	0.250(2)	0.0349(4)	0.48
O3	1	4e	0	0.227(2)	0.25	0.48
O4	1	8f	0.2703(4)	0.740(2)	0.0811(3)	0.48
O5	1	8f	0.4480(4)	0.746(2)	0.0734(4)	0.48
O6	1	8f	0.1842(3)	0.257(2)	0.2221(3)	0.48

(a) $Pb_2Ti_4O_9F_2$ (300 K)

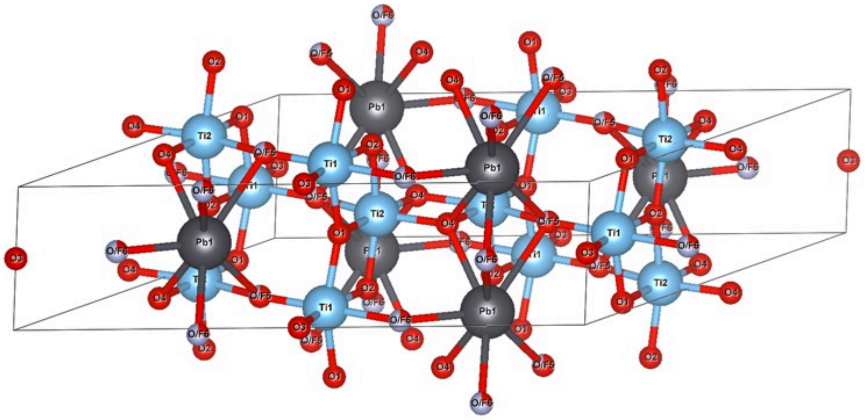

(b) $Bi_2Ti_4O_{11}$ (600 K)

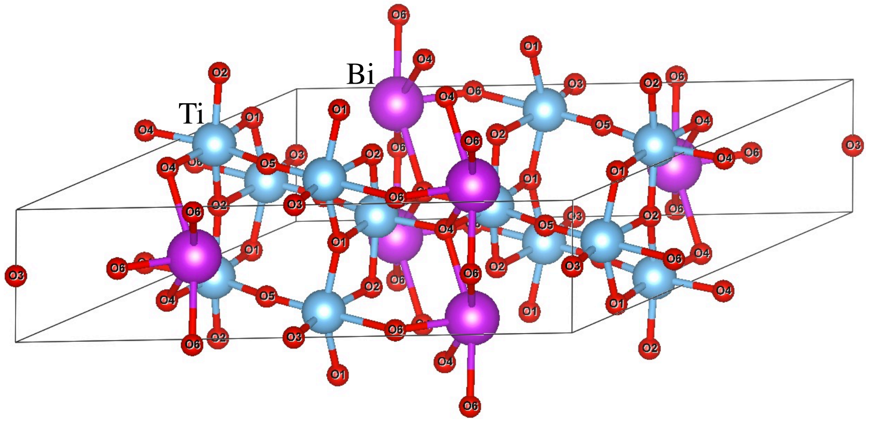

(c) $Bi_2Ti_4O_{11}$ (300 K)

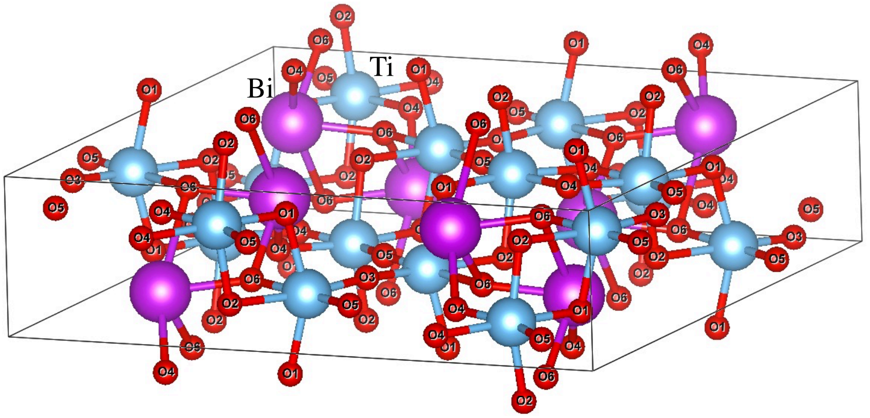

Figure S2: Visualization of crystal structures and anion sites.

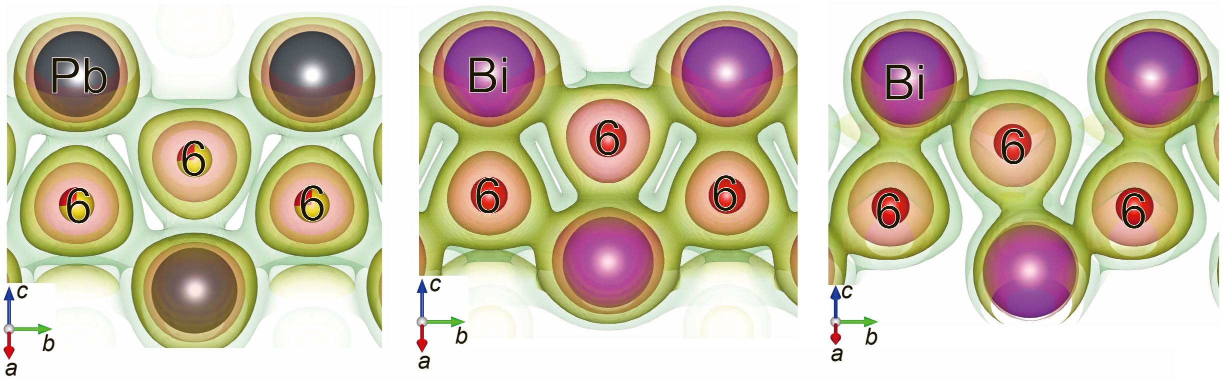

$Pb_2Ti_4O_9F_2$ (300 K) *C2/m* $Bi_2Ti_4O_{11}$ (600 K) *C2/m* $Bi_2Ti_4O_{11}$ (300 K) *C2/c*

Figure S3: Electron density distributions obtained by MEM for $Pb_2Ti_4O_9F_2$ and $Bi_2Ti_4O_{11}$. The isosurface levels for 2 $e/\text{Å}^3$, 4 $e/\text{Å}^3$ and 12 $e/\text{Å}^3$ are shown in green, yellow and red colors, respectively.

anisotropic change in covalency around Bi^{3+} is associated with the anti-parallel displacement of Bi^{3+} ion along the *b* axis. This potentially suggests $6s^2$ lone pair electrons at play, because such a huge displacement accompanied by the anisotropic change in covalency is not found in typical oxides. This anti-parallel displacement is considered to be the origin of antiferroelectric transition of $Bi_2Ti_4O_{11}$.[1] This transition is similar to the case of some Aurivillus oxides $ABi_2Nb(Ta)_2O_9$[2–4] those show a ferroelectric–paraelectric transition, which is considered to be a consequence of a distortion by $6s^2$ lone pairs.[2]

Details of through-space correlation NMR experiments

The pulse sequence used for through-space correlation experiments was shown in S4. The delay time T_{CSF} of half the reciprocal of the chemical shift difference in Hz units after the excitation pulse selectively inverts the magnetization of 19F at −45 ppm. After the chemical-shift filter, the flipback pulse returns the magnetization to the z-axis. After a mixing time T_{mix} the magnetization was corrected with the background suppression pulses. When the integer multiples of spinning rate match to the difference in chemical shifts of a homonuclear spin pair, rotational resonance occurs, where the dipolar interaction is restored. Thus, using rotational resonance, we can confirm

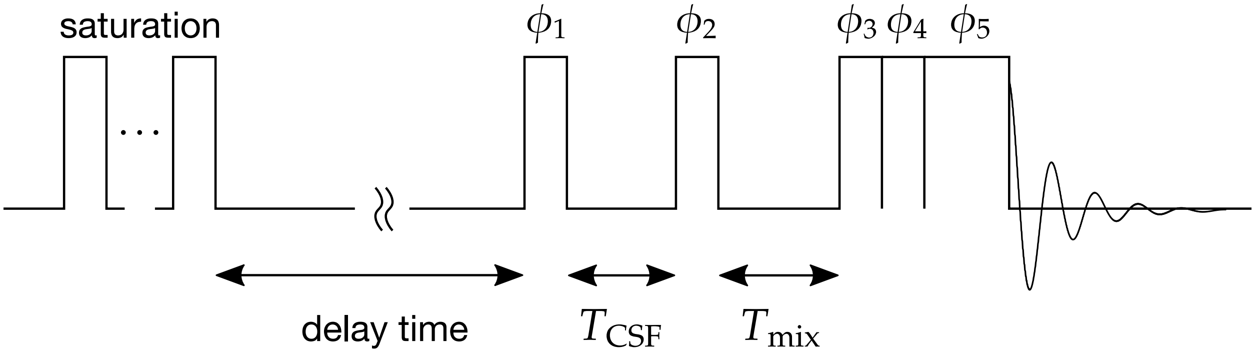

Figure S4: The pulse sequence used to confirm whether ^{19}F atoms of the two main peaks exist in the same crystal phase. The thin and thick vertical rectangles represent the $\pi/2$ and π pulses with the phases represented as ϕ. T_{CSF} is a delay time for chemical shift filter and T_{mix} is a mixing time. Here, we set $T_{\mathrm{CSF}} = 132$ µs and $T_{\mathrm{mix}} = 0, 20, 40, 60, 80, 100$ µs. Only the restored magnetization through rotational resonance to ^{19}F can be acquired with background suppression by setting the phase cycling of the pulses and a receiver as follows: $\phi_1 = \{y, -y\}$; $\phi_2 = \{-y\}$; $\phi_3 = \{x, x, -x, -x, -y, -y, y, y, -x, -x, x, x, y, y, -y, -y, x, x, -x, -x, -y, -y, y, y, -x, -x, x, x, y, y, -y, -y\}$; $\phi_4 = \{x, x, -x, -x, -y, -y, y, y, -y, -y, y, y, -x, -x, x, x, -x, -x, x, x, y, y, -y, -y, y, y, -y, -y, x, x, -x, -x\}$; $\phi_5 = \{x, x, -y, -y, y, y, x, x, -y, -y, x, x, x, x, y, y, x, x, -y, -y, y, y, x, x, -y, -y, x, x, x, x, y, y\}$; receiver $= \{x, -x, x, -x, -y, y, -y, y, -x, x, -x, x, y, -y, y, -y, x, -x, x, -x, -y, y, -y, y, -x, x, -x, x, y, -y, y, -y\}$.

whether the spins of ^{19}F appearing at −63 ppm and −45 ppm peaks are coupled or not through dipolar interaction.

Figure S5 shows the ^{19}F MAS NMR spectra at 4.7 T by using the pulse sequence shown in Fig. S4. By adjusting the spinning rate at ca. 3.7 kHz, the magnetization was restored through rotational resonance between the two peaks. The intensity of the two peaks oscillate with increasing T_{mix}. On the other hand, when the spinning rate was sufficiently high, no oscillation of the peak intensity was observed with increasing T_{mix}.

References

(1) Kahlenberg, V.; Böhm, H. The structures of α- and β-Bi2Ti4O11. Acta Crystallographica Section B Structural Science **1995**, 51, 11–18.

(2) Ismunandar,; Kennedy, B. J.; Gunawan,; Marsongkohadi, Structure ofABi2Nb2O9(A= Sr,

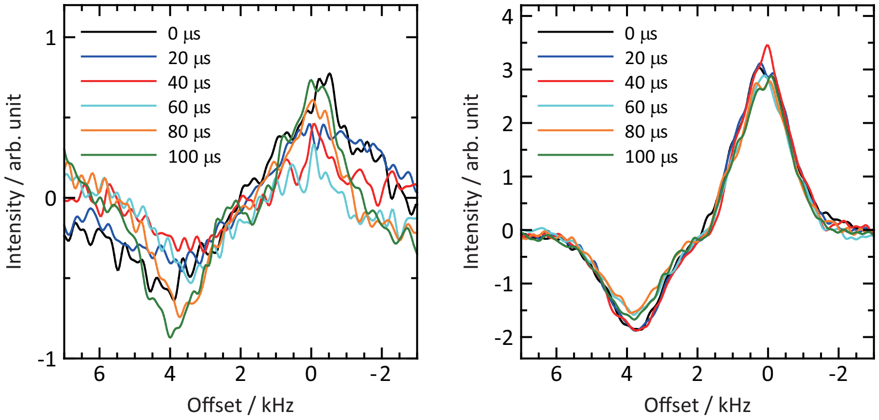

Figure S5: ^{19}F MAS NMR spectra obtained at 4.7 T by using the pulse sequence shown in Fig. S4 obtained with a MAS rate of ca. 3.7 kHz (left) and ca. 12 kHz as a control (right).

Ba): Refinement of Powder Neutron Diffraction Data. Journal of Solid State Chemistry **1996**, 126, 135–141.

(3) Subbarao, E. A family of ferroelectric bismuth compounds. Journal of Physics and Chemistry of Solids **1962**, 23, 665–676.

(4) Shimakawa, Y.; Kubo, Y.; Nakagawa, Y.; Goto, S.; Kamiyama, T.; Asano, H.; Izumi, F. Crystal structure and ferroelectric properties of $A\mathrm{Bi_2Ta_2O_9}$(A = Ca, Sr, and Ba). Phys. Rev. B **2000**, 61, 6559–6564.